THE JOURNAL OF PHYSICAL CHEMISTRY C

Article

Cite This: J. Phys. Chem. C 2018, 122, 28423−28430

pubs.acs.org/JPCC

Extraordinary Magnetoresistance in Janus Monolayer $MoTeB_2$: A Theoretical Prediction

Shijun Yuan,[†,‡] Hui Ding,[†] Jinlan Wang,*[,†] and Zhongfang Chen*[,‡]

[†]School of Physics, Southeast University, Nanjing 211189, P.R. China

[‡]Department of Chemistry, University of Puerto Rico, Rio Piedras Campus, San Juan, PR 00931, United States

Supporting Information

ABSTRACT: By means of first-principles calculations, we investigated the geometric structure, dynamic and thermal stabilities, and electronic properties of the two-dimensional (2D) Janus group III chalcogenide monolayer $MoTeB_2$. The $MoTeB_2$ monolayer exhibits a stable sandwiched structure, and its semimetal electronic structure features the perfect electron−hole compensation. The 1:1 electron−hole carrier ratio and high carrier mobility endow the $MoTeB_2$ monolayer with large and nonsaturating magnetoresistance. Its electronic properties are easily adjustable by minute charge doping and small tensile stains; in particular, the switch of carrier polarity and metal−semiconductor phase transformation can be achieved. This study not only leads to the finding of the Janus $MoTeB_2$ monolayer as a promising 2D material with extraordinary magnetoresistance but also provides a general route to adjust the magnetoresistance effect by compressive stain and charge doping.

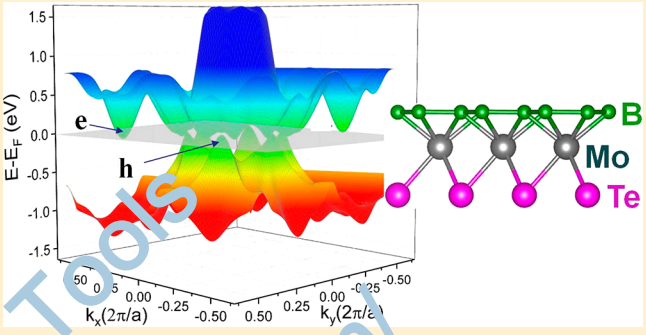

I. INTRODUCTION

Materials with large magnetoresistance effect have promising applications such as magnetic memory,[1] magnetic information storage,[2] and magnetic sensors.[3] Compared to giant magnetoresistance (GMR) and colossal magnetoresistance (CMR) effect, ordinary magnetoresistance (OMR) is usually a relatively weak effect. Typically, the OMR effect of nonmagnetic metal is at the level of 1%, quadratic only in low field, and tends to saturate in high magnetic field.[4] However, an extremely large magnetoresistance has been found in several semimetal materials, such as $PdCoO_2$, WTe_2, Cd_3As_2, $NbSb_2$, and $MoTe_2$.[5−9] Remarkably, Ali et al. discovered a 450 000-fold OMR in the quasi-two-dimensional WTe_2 layered crystal in a magnetic field of 14.7 T at 4.5 K, and no saturation of OMR even in 60 T.[6]

Classically, the GMR and CMR effects in magnetic multilayers and manganese-based perovskite oxides are attributed to the electron scattering on the spin orientation.[1,2] In contrast, different mechanisms have been proposed to explain the extremely large OMR effect in different nonmagnetic compounds.[10] One explanation is based on the classical two-band model,[4] according to which the electron−hole compensation is the determining factor for the nonsaturating magnetoresistance in high magnetic field. For example, the equal-size electron and hole Fermi pockets have been observed in WTe_2 by angle-resolved photoemission spectroscopy.[11] The alternative explanation, however, argues that the high mobility is the key to the extremely large OMR effect; that is, materials having electrons or holes with ultrahigh mobility but without balanced electron−hole concentrations can also possess a large OMR effect.[5,7,8,12] A typical example is the $NbSb_2$ bulk, which has a small amount of high-mobility hole carrier and a large amount of low-mobility electron carrier.[8] Regardless of the preferred mechanism, we can expect that a material satisfying both perfect electron−hole compensation and high mobility for two-type carriers will undoubtedly exhibit an extremely large and nonsaturated magnetoresistance effect.

A strategy for searching for extremely large OMR materials can start from the perspective of high carrier mobility, followed by good electron−hole compensation. Some two-dimensioanl (2D) materials with hexagonal boron rings have been predicted to hold ultrahigh carrier mobility, such as TiB_2, FeB_2, and MoB_4.[13−15] However, though these materials have high mobility because of the Dirac cone, the electron carriers and hole carriers cannot coexist; thus, the electron−hole compensation is impossible. Breaking the structural symmetry may provide a possible solution to this problem. Specifically, the increased structural freedom may lead to separated positions of electron-type and hole-type energy bands in the Brillouin zone, while retaining the feature of high carrier mobility. Encouragingly, several sophisticated experimental methods have been developed to break the mirror symmetry of 2D materials in the out-of-plane direction, among which the realization of Janus graphene[16] and Janus MoSSe[17,18] are shining examples. For example, Lu et al. successfully prepared 2D Janus transition-

Received: October 24, 2018
Revised: November 19, 2018
Published: November 20, 2018

DOI: 10.1021/acs.jpcc.8b10371
J. Phys. Chem. C 2018, 122, 28423−28430

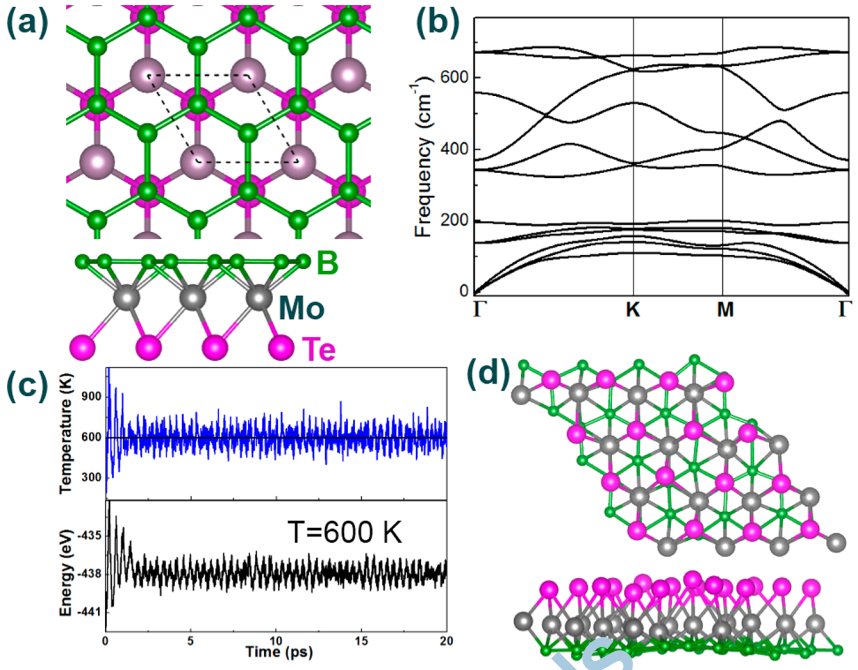

Figure 1. Structure and stability of $MoTeB_2$. (a) Top and side views of relaxed structure. (b) Phonon dispersion curves. (c) Temperature/energy fluctuations vs simulation time in molecular dynamics simulations at 600 K, and (d) the snapshot of a (4 × 4) supercell of $MoTeB_2$ monolayer after a 20 ps molecular dynamics (MD) simulation.

metal dichalcogenides MoSSe by H_2-plasma-stripping techniques in which the top-layer S atoms of MoS_2 are fully replaced by Se atoms.[17] Subsequent studies revealed that this material has exceptional electronical,[19−22] optical,[23,24] and photocatalytic properties[25,26] because of its unique structural properties. Therefore, 2D planar-boron-based Janus material may have the potential to possess extremely large OMR.

Herein, by means of first-principles calculations, we designed a 2D Janus material, namely, $MoTeB_2$ monolayer, and systematically investigated its stability and electronic properties. Interestingly, the $MoTeB_2$ monolayer is a semimetal with high mobility for both electrons and holes, and its electronic structure is featured by the perfect electron−hole compensation. Moreover, its electronic properties are easily adjustable by minute charge doping and/or small tensile stains. In particular, the 1:1 electron−hole carrier ratio and high carrier mobility can be well-maintained regardless of external strain. These unique properties render the $MoTeB_2$ monolayer a promising 2D material with extraordinary magnetoresistance.

II. COMPUTATIONAL METHOD

Spin-polarized density functional theory (DFT) computations were carried out using the Vienna ab initio simulation package (VASP) code[27,28] within the projector augmented-wave (PAW) method.[29] The Perdew−Burke−Ernzerhof (PBE) exchange-correlation functional within the generalized gradient approximation (GGA) were adopted.[30] The wave energy cutoff of plane-wave basis sets is 500 eV. A vacuum space of at least 15 Å along the out-of-plane direction was employed to ensure that the interactions between periodic images are negligible. The Monkhorst−Pack 35 × 35 × 1 *k*-point sampling for a primitive cell was used for both geometry optimization and electronic calculations. The lattice constants and atomic coordinates were fully relaxed until the total energy and force converged to 10^{-7} eV and to 10^{-3} eV/Å, respectively. The phonon frequencies were calculated with 4 × 4 × 1 supercell and 7 × 7 × 1 *k*-meshes by using density functional perturbation theory[31] as implemented in the PHONOPY code.[32] The ab initio molecular dynamics (AIMD) simulations under a constant-temperature and volume (NVT) ensemble were performed with a supercell of 4 × 4 × 1 unit cells, for which the total simulation time lasts for 20 ps with 1 fs time step.

III. RESULTS AND DISCUSSION

A. Optimized Structure and Stability of the $MoTeB_2$ Monolayer. The optimized $MoTeB_2$ monolayer can be viewed as the sandwiched Te−Mo−B trilayer, with two B atoms, one Te atom, and one Mo atom per unit cell (Figure 1a). The Janus $MoTeB_2$ monolayer can also be regarded as a hexagonal boron lattice sequentially covered by a triangular Mo layer and a triangular Te layer. In the optimized structure, B atoms are arranged in a slightly buckled honeycomb lattice with a height of 0.02 Å, and Te and Mo atoms are in purely planar trigonal lattices, with Te atoms located on the top of B atoms and Mo atoms above the center of the B hexagons. The B−B bond length (1.81 Å) is between that in a free-standing boron honeycomb (1.67 Å)[33] and that in the PS_B-type MoB_4 bulk (1.85 Å).[34] The Mo−B and Mo−Te bond lengths (2.34 and 2.74 Å, respectively) are similar to the Mo−B bond (2.37 Å) in MoB_4 monolayer[15] and the Mo−Te bond (2.71 Å) in 2H-$MoTe_2$ monolayer.[35]

To evaluate the dynamical stabilities of $MoTeB_2$ monolayer, we computed its phonon dispersion. The absence of any imaginary frequency (Figure 1b) strongly suggests that the $MoTeB_2$ monolayer is a local minimum in its energy landscape. Then we performed AIMD simulation at 600 K for 20 ps to evaluate the thermal stability of $MoTeB_2$ monolayer. The $MoTeB_2$ sheet keeps quite original planarity without significant lattice destruction at 600 K [see Figure 1d], and begins to collapse at 800 K (Figure S1, Supporting Information), which strongly suggests its thermal stability.

DOI: 10.1021/acs.jpcc.8b10371
J. Phys. Chem. C 2018, 122, 28423−28430

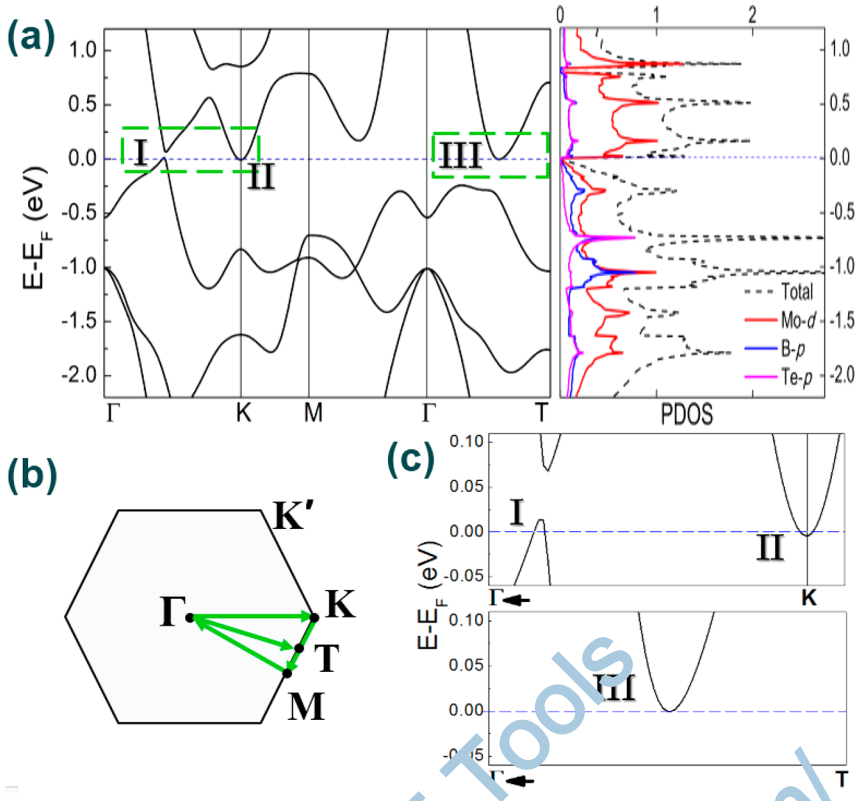

Figure 2. (a) Electronic band structure and projected density of states (PDOS) for $MoTeB_2$. (b) First Brillouin zone and high-symmetry points along the band structure path for $MoTeB_2$. (c) Details of the calculated electronic structure in the Γ−K and Γ−T directions, which are amplified versions of the dashed green boxes in Figure 2a. Three regions where the energy bands traverse the Fermi level (E_F) are labeled by I, II, and III.

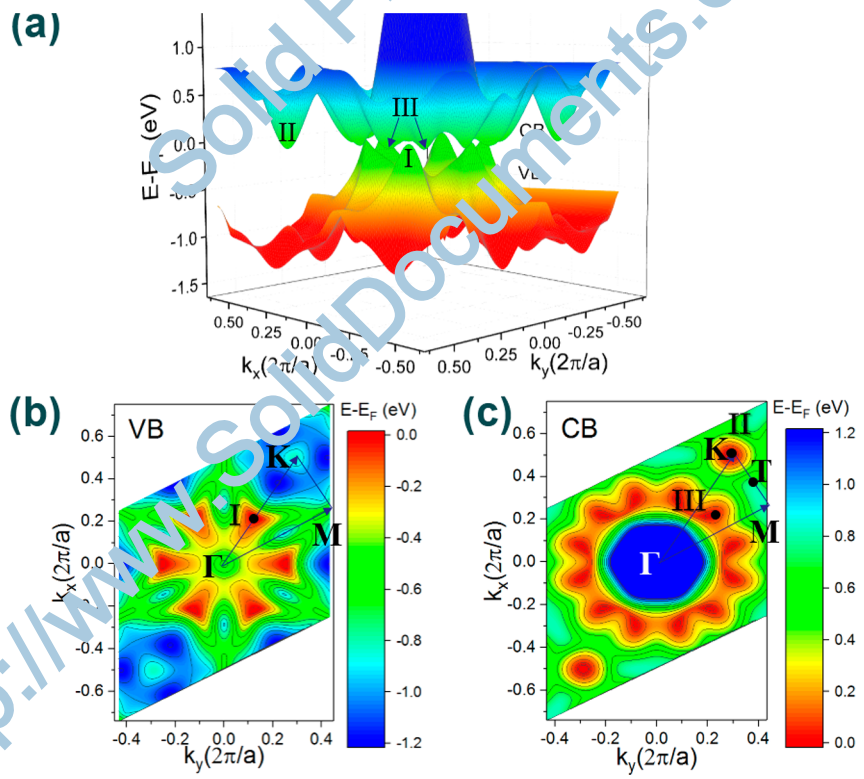

Figure 3. (a) 3D conduction band (CB) and valence band (VB) of $MoTeB_2$. The constant-energy contours for (b) VB and (c) CB. The black dots at $E - E_F = 0.0$ eV labeled as Regions I, II, and III, the same as in Figure 2.

B. Electronic Properties of the $MoTeB_2$ Monolayer. The $MoTeB_2$ monolayer is semimetal, with the valence band (VB) and the conduction band (CB) barely crossing the Fermi level. The two regions where the energy bands flip over the Fermi level

DOI: 10.1021/acs.jpcc.8b10371
J. Phys. Chem. C 2018, 122, 28423−28430

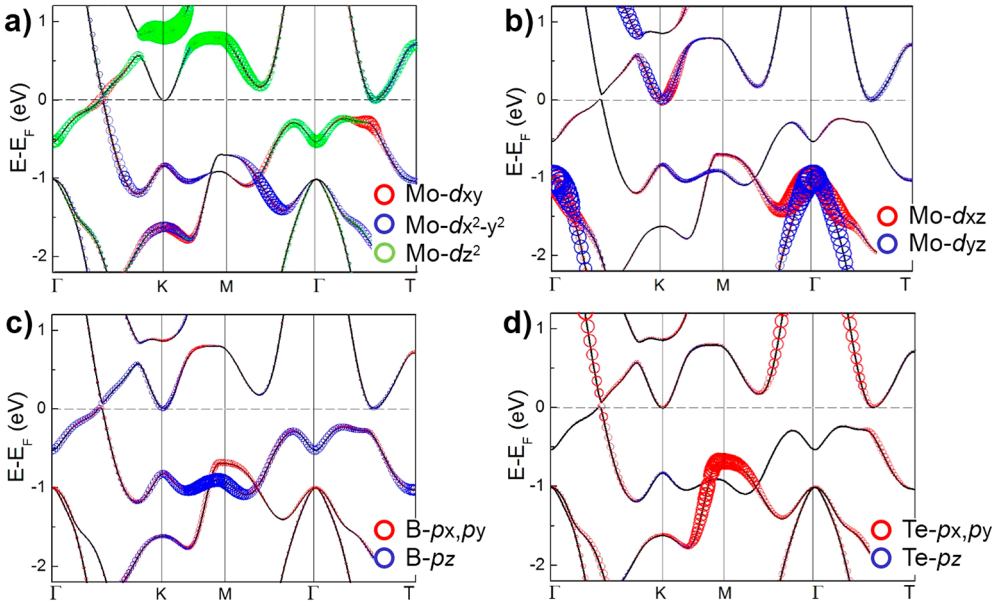

Figure 4. Projected band structures of $MoTeB_2$. (a) and (b) d orbitals of Mo atom, (c) p orbitals of B atom, and (d) p orbitals of Te atom. The radii of circles are proportional to the weights of corresponding orbitals.

are denoted as Region I and Region II in the Brillouin zone, as shown in Figure 2a. The projected density of states indicate that the states near the Fermi level mainly receive contributions from the d orbitals of Mo, with insignificant contributions from p orbitals of B and Te atoms. The VB and CB almost meet in Region I with a tiny gap of 0.05 eV (see Figure 2c). The hole-type band around Region I along the Γ−K direction is the valence band maximum (VBM), whereas the electron-type band around K point (Region II) is the conduction band minimum (CBM). Such a unique electronic property stems from the delicate relative positions between the CBM and the VBM; that is, the VBM is only 17 meV higher than the CBM, which results in its semimetal feature. Meanwhile, there is a contact point between the CB and Fermi level, located in Region III in Figure 2a. The CB is tangent to the Fermi energy level (in Region III) along the Γ−T direction, where the T point is the middle point between the high symmetric points M and K, as shown in Figure 2b. Furthermore, the details of energy bands near the Fermi level are not affected by spin−orbit coupling effect, as shown in Figure S2.

To understand the relative position of energy bands near the Fermi level in the reciprocal space, we plot the three-dimensional VB and CB in the first Brillouin zone, as shown in Figure 3a. The energy peaks of VB (Region I) with sixfold symmetry lie right between two energy valleys (Region III) of CB: the six VB peaks and the 12 CB valleys occlude like gears, but do not touch each other. Both VB and CB have the same D_6 symmetry, which is due to the hexagonal lattice symmetry ($p6m$) of $MoTeB_2$ structure.

The transport properties of metal materials are determined by the energy bands passing through the Fermi level. Thus, we examined the energy bands of $MoTeB_2$ in Regions I and II in more detail. As shown in Figure 3b,c, the 2D energy contours of VB and CB exhibit different morphologies for the hole-type band and the electron-type band near the Fermi level. The contour lines around VBM (Region I) are of remarkable anisotropy. The calculated slopes of VB along the Γ−I direction and the I−K direction in the reciprocal space are equal to 6.7 and −30 eV·Å, respectively. Such steep slopes are comparable to even the linear slope of ±34 eV·Å at the Dirac point in graphene,[36] indicating the rather high hole mobility of $MoTeB_2$ monolayer.

These direction-dependent slopes are related to the different orbital compositions in VB. As shown in Figure 4a,c, the VB exhibits a gentle linear energy dispersion in the Γ−I direction, which mainly receive contributions from the hybrid of Mo d_{z^2} orbitals and B p_z orbitals. In comparison, the linear energy dispersion of VB in the I−K direction is sharp, and this hole-type band mainly receives contributions from the hybrid of Mo $d_{x^2-y^2}$ orbitals and Te p_x,p_y orbitals, as shown in Figure 4a,d. The different slopes of VB along two directions could be understood by the different interaction strengths: the sharp VB in the I−K direction stems from the stronger interaction between Mo and Te layers, which can be attributed to the more effective hybridization between Mo and Te atomic orbitals. Moreover, the projected band structure around Region I also reveals the origin of the tiny energy gap, that is, the absence of the hybridization between the Te p_x,p_y orbitals and the B p_z orbital.

As discussed above, the hole-type VB is anisotropic; in contrast, the electron-type CB is isotropic around the high symmetric point K, as shown in Figure 3c. The quadratic energy band near the Fermi level mainly receives contributions from the hybrid of Mo d_{xz},d_{yz} orbitals and B p_z orbitals (Figure 4b,c), while the contribution of Te atoms is negligible.

The above analysis of the projected bands and 2D energy contours near the Fermi level clearly reveal that the electron-type band and hole-type band stem from different sub-bilayers in the Janus $MoTeB_2$ sandwich. Specifically, the electron-type carriers of CB come only from the hybridization between Mo layer and B layer, while the hole-type carriers of VB originate from the hybridization of Mo layer, Te layer, and B layer. Because of the sharp energy dispersion of the electron-type band and the hole-type band, the high carrier mobility can be expected in the $MoTeB_2$ monolayer. In particular, its electronic structure exhibits almost perfectly balanced electron−hole population, which strongly indicates that the $MoTeB_2$ monolayer has a very high and nonsaturating magnetoresistance effect for electron−hole resonance.

DOI: 10.1021/acs.jpcc.8b10371
J. Phys. Chem. C 2018, 122, 28423−28430

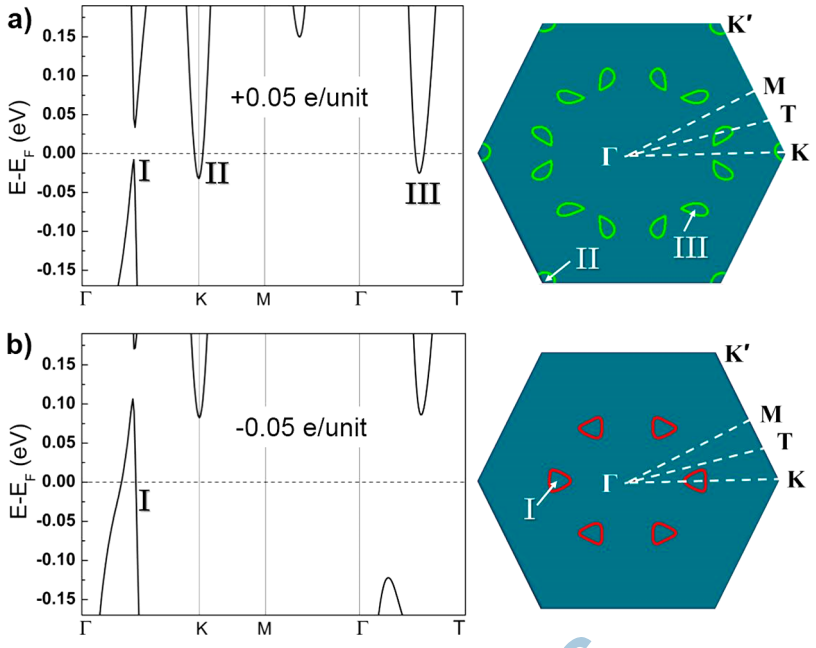

Figure 5. Band structures and Fermi surface of $MoTeB_2$ doped with electrons or holes: (a) 0.05 electron doping and (b) 0.05 hole doping per unit cell.

C. Estimation of Magnetoresistance Value of $MoTeB_2$ Monolayer. Magnetoresistance (MR) is defined as $(\rho(H) - \rho_0)/\rho_0$, where $\rho(H)$ and ρ_0 are the resistivity with and without external magnetic field H, respectively. In the semiclassical two-band model, the total conductivity tensor can be expressed as

$$\hat{\sigma} = \frac{1}{\hat{\rho}} = e\left[\frac{n\mu_e}{(1 + i\mu_e B)} + \frac{p\mu_h}{(1 - i\mu_h B)}\right] \quad (1)$$

where n and p are the electron and hole concentrations, respectively, and μ_e and μ_h are the mobilities of electrons and holes, respectively. So the magnetoresistance can be expressed as

$$\mathrm{MR} = \frac{\sigma_e\sigma_h(\sigma_e/n + \sigma_h/p)^2(B/e)^2}{(\sigma_e + \sigma_h)^2 + \sigma_e^2\sigma_h^2(1/n - 1/p)^2(B/e)^2} \quad (2)$$

where $\sigma_e = ne\mu_e$ and $\sigma_h = pe\mu_h$ are the conductivities of electrons and holes without magnetic field. When the electron−hole concentraions are at exact compensation ($n = p$), the MR = $\mu_e\mu_h B^2$ increases as B^2 without saturation. Therefore, to obtain remarkable MR at specific magnetic field, the high carrier mobility is desirable.

By the deformation potential model, the room-temperature μ_e and μ_h of $MoTeB_2$ monolayer are calculated to be 5.9×10^4 and 2.0×10^5 $cm^2\ V^{-1}\ s^{-1}$, respectively (for the details including effective masses, elastic modulus, and the deformation potential constants, refer to Table S1). Note that the computed carrier mobilities in $MoTeB_2$ monolayer are even larger than those in WTe_2 monolayer[37] ($\mu_e = 1.3 \times 10^4$ $cm^2\ V^{-1}\ s^{-1}$, $\mu_h = 2.1 \times 10^4$ $cm^2\ V^{-1}\ s^{-1}$, respectively), which is the only experimentally observed nonsaturating OMR material.[6] The exceptionally high carrier mobilities of $MoTeB_2$ monolayer is attributed to rather small effective masses of electron-type band and the almost linear hole-type band near the Fermi surface. Therefore, the $MoTeB_2$ monolayer possesses rather large and nonsaturating magnetoresistance because of the electron−hole compensation and the high carrier mobilities.

Considering the delicate electronic properties of the $MoTeB_2$ monolayer, we also examined its band structure (Figure S5 in the Supporting Information) using the Heyd−Scuseria−Ernzerhof (HSE06)[38] hybrid functional. At HSE06 level of theory, the shape of electron-type and hole-type bands is essentially the same as that obtained at GGA-PBE, though a narrow band gap (117 meV) is introduced at HSE because of the upshift of conduction bands. Consequently, the high electron and hole carrier mobilities obtained at PBE hold true also at HSE level of theory. Thus, the unsaturated magnetoresistance characteristic can also be expected in $MoTeB_2$ monolayer when the hybrid HSE06 functional is used, providing that the band smearing at the finite temperature is considered.

D. Charge-Doped $MoTeB_2$ Monolayer. In nanoscale semiconductor devices, the electrostatic doping or gate-controlled doping are effective methods to modulate the electron and hole concentrations.[39,40] To achieve extremely large OMR effect, it is highly important to adjust the electron−hole concentration ratio.

In $MoTeB_2$ monolayer, because of the rather sharp electron-type band and hole-type band around the Fermi level, even minute charge doping can cause a significant Fermi level shift. Interestingly, after electron or hole doping, the band structures of the $MoTeB_2$ monolayer is still metallic, but the carrier polarity is switched (Figure 5). For electron doping, only the electron-type Fermi lines exist in the $MoTeB_2$ monolayer, while the hole-type Fermi lines vanish. As shown in Figure 5a, upon doping 0.05e per $MoTeB_2$ unit cell, the CB in Regions II and III shifts down below the Fermi level, keeping 12 drop-shape Fermi lines in Region III and one circular Fermi ring around the K point in the first Brillouin zone. In comparison, upon doping 0.05e hole per $MoTeB_2$ unit cell, the polarity of carriers turns to hole-type, and the band structure is rather anisotropic, as indicated by the six trilateral hole-type Fermi lines in Region I, as shown in Figure 5b. Interestingly, regardless of the type of charge injection, the $MoTeB_2$ monolayer preserves the high hole or electron mobility, which is beneficial to the large OMR effect.

E. Strained $MoTeB_2$ Monolayer. The external strain is an effective method to manipulate the electronic properties of low-dimensional materials;[41] thus, we further investigated the strain effect on the $MoTeB_2$ monolayer. Clearly, under isotropic in-

DOI: 10.1021/acs.jpcc.8b10371
J. Phys. Chem. C 2018, 122, 28423−28430

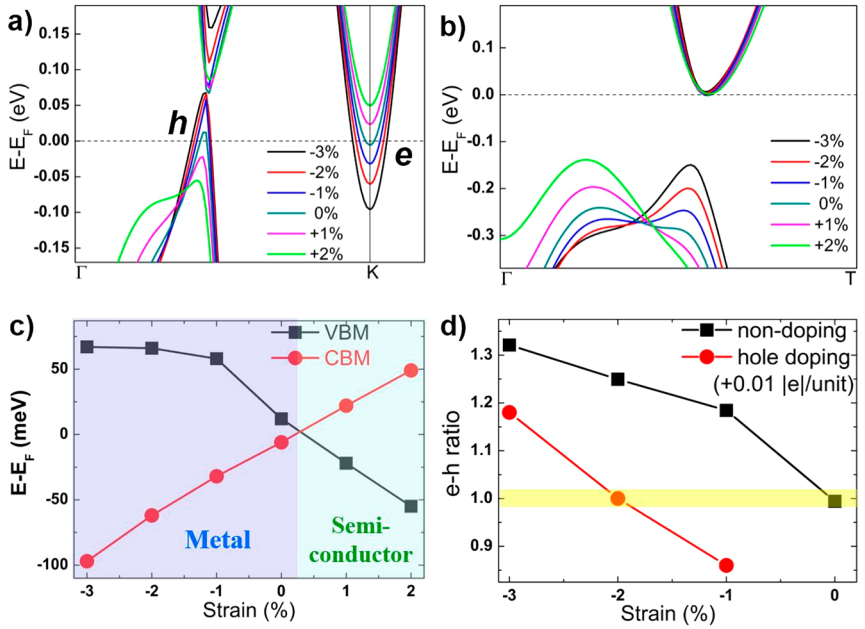

Figure 6. Band structures of $MoTeB_2$ in the (a) Γ−K and (b) Γ−T directions under different biaxial strains (from −3% compress to +2% stretch). The hole and electron bands are marked with *h* and *e*, respectively. (c) The energy of VBM and CBM under external strains. (d) Strain-dependent concentration ratios of electron-type carrier and hole-type carrier without and with hole doping. The yellow area highlights the *e*−*h* ratio within 1.00 ± 2%.

plane strains, obvious energy shift of the hole-type and electron-type bands appears in Regions I and II (Γ−K direction) of the band structure (Figure 6a), but the electron-type band in Region III (Γ−T direction) is insensitive to deformation, and it always tangential to the Fermi level under different strains (Figure 6b). Thus, we will focus only on the changes of the hole- and electron-band along the Γ−K direction.

Remarkably, semimetal−semiconductor transformation occurs in the $MoTeB_2$ monolayer upon tensile strains. Because of different responses of the hole-type band in Regions I and the electron-type band around the point K, the energies of CBM and VBM move up and down, respectively (Figure 6c). The $MoTeB_2$ monolayer can be easily transformed from a semimetal to an indirect narrow band gap semiconductor with a tensile strain greater than 0.2%. In contrast, in the case of compressive strain the $MoTeB_2$ monolayer keeps the semimetal feature. Upon compressive strains from 0% to −3%, the CBM moves down linearly and rapidly, while the VBM shifts up quickly and then saturates to 67 meV (see the black line in Figure 6c). Since the CBM and VBM behave differently under external compressive strain, the electron−hole concentration ratio can be tailored, which is essential for the emergence of extremely large OMR effect.

As aforementioned, the neutral and unstrained $MoTeB_2$ monolayer is rather promising as a 2D OMR material because of its high carrier mobility and perfectly balanced electron−hole concentration. Providing that the unique electron−hole balance can be maintained in the presence of external stress, the $MoTeB_2$ monolayer may be widely used on realistic substrates. Thus, we investigated the electron−hole concentration ratios under different strains.

To quantitatively evaluate the electron−hole ratio, we first calculated the total perimeters of the electron-type Fermi lines (around point K) and the hole-type Fermi lines (in Region I) in the Brillouin zone. Then the concentration radio of two types of carriers can be obtained from the perimeter ratios because the carrier concentrations are proportional to the total lengths of Fermi lines.

Figure 6d summarizes the calculated electron−hole ratios under various external strains. With increasing compressive strain, the electron concentration increases faster than the hole concentration, for example, the electron−hole ratio reaches 1.25:1 at the −2% compressive strain (Figure 6d). Nevertheless, this unbalanced electron−hole concentration can be adjusted back to the electron−hole compensation by a slight hole doping of +0.01 |e| per $MoTeB_2$ unit cell. Thus, the $MoTeB_2$ monolayer can maintain the large OMR effect under various compressive strains, if suitable hole doping is applied.

CONCLUSIONS

In summary, we designed a Janus $MoTeB_2$ monolayer, and systematically examined its geometric structure, stability, electronic properties, and the strain effect and charge-doping effect by means of DFT computations. The $MoTeB_2$ monolayer has outstanding dynamic and thermal stabilities, and is semimetal with CB and VB barely crossing the Fermi level. Its electronic property is sensitive to charge doping because of the sharp energy dispersions. The carrier polarity can be switched between electron-type and hole-type by a slight charge doping. Moreover, the electron−hole carrier ratio can be modulated by external strains, and the metal−semiconductor transition occurs under tensile stain. Appropriate hole doping can effectively achieve the 1:1 electron−hole ratio in the strained $MoTeB_2$ monolayer. Because of its peculiar and adjustable electronic properties, the $MoTeB_2$ monolayer is a promising material for magnetoresistance nanodevice applications.

ASSOCIATED CONTENT

Supporting Information

The Supporting Information is available free of charge on the ACS Publications website at DOI: 10.1021/acs.jpcc.8b10371.

DOI: 10.1021/acs.jpcc.8b10371
J. Phys. Chem. C 2018, 122, 28423−28430

The computational data and methods for carrier mobilities of different 2D materials, the structural dynamic stability of $MoTeB_2$ under strain, AIMD snapshots at 700 and 800 K, and band structure with spin−orbit coupling for $MoTeB_2$, band structures of $MoTeB_2$ with vacancy defects, and band structure of MoTeB2 monolayer by HSE06 functional (PDF)

AUTHOR INFORMATION

Corresponding Authors

*E-mail: jlwang@seu.edu.cn (J.W.).
*E-mail: zhongfangchen@gmail.com (Z.C.).

ORCID

Shijun Yuan: 0000-0001-7097-9662
Jinlan Wang: 0000-0002-4529-874X
Zhongfang Chen: 0000-0002-1445-9184

Notes

The authors declare no competing financial interest.

ACKNOWLEDGMENTS

This work is supported in China by the National Key R&D Program of China (Grant No. 2017YFA0204800), Natural Science Funds of China (21525311, 21773027), Jiangsu 333 project (BRA2016353), and in USA by NSF-CREST Center for Innovation, Research and Education in Environmental Nanotechnology (CIRE2N) (Grant No. HRD-1736093). S.J.Y. gratefully acknowledges financial support from the China Scholarship Council. This research used resources of the High Performance of Computational facility (HPCf), University of Puerto Rico, which is partially supported by an Institutional Development Award (IDeA) INBRE Grant Number P20GM103475 from the National Institute of General Medical Sciences (NIGMS), a component of the National Institutes of Health (NIH), and the Bioinformatics Research Core of the INBRE. Its contents are solely the responsibility of the authors and do not necessarily represent the official view of NIH.

REFERENCES

(1) Moritomo, Y.; Asamitsu, A.; Kuwahara, H.; Tokura, Y. Giant magnetoresistance of manganese oxides with a layered perovskite structure. *Nature* **1996**, *380*, 141.
(2) Prinz, G. A. Magnetoelectronics. *Science* **1998**, *282*, 1660−1663.
(3) Daughton, J.; Brown, J.; Chen, E.; Beech, R.; Pohm, A.; Kude, W. Magnetic field sensors using GMR multilayer. *IEEE Trans. Magn.* **1994**, *30*, 4608−4610.
(4) Pippard, A. B. *Magnetoresistance in Metals*; Cambridge University Press: Cambridge, England, 1989.
(5) Takatsu, H.; Ishikawa, J. J.; Yonezawa, S.; Yoshino, H.; Shishidou, T.; Oguchi, T.; Murata, K.; Maeno, Y. Extremely large magnetoresistance in the nonmagnetic metal $PdCoO_2$. *Phys. Rev. Lett.* **2013**, *111*, 056601.
(6) Ali, M. N.; et al. Large non-saturating magnetoresistance in WTe_2. *Nature* **2014**, *514*, 205.
(7) Liang, T.; Gibson, Q.; Ali, M. N.; Liu, M.; Cava, R. J.; Ong, N. P. Ultrahigh mobility and giant magnetoresistance in the Dirac semimetal Cd_3As_2. *Nat. Mater.* **2015**, *14*, 280.
(8) Wang, K.; Graf, D.; Li, L.; Wang, L.; Petrovic, C. Anisotropic giant magnetoresistance in $NbSb_2$. *Sci. Rep.* **2015**, *4*, 7328.
(9) Pei, Q. L.; Meng, W. J.; Luo, X.; Lv, H. Y.; Chen, F. C.; Lu, W. J.; Han, Y. Y.; Tong, P.; Song, W. H.; Hou, Y. B.; Lu, Q. Y.; Sun, Y. P.; et al. Origin of the turn-on phenomenon in T_d−$MoTe_2$. *Phys. Rev. B: Condens. Matter Mater. Phys.* **2017**, *96*, 075132.
(10) Yuan, Z.; Lu, H.; Liu, Y.; Wang, J.; Jia, S. Large magnetoresistance in compensated semimetals $TaAs_2$ and $NbAs_2$. *Phys. Rev. B: Condens. Matter Mater. Phys.* **2016**, *93*, 184405.
(11) Pletikosić, I.; Ali, M. N.; Fedorov, A. V.; Cava, R. J.; Valla, T. Electronic Structure Basis for the Extraordinary Magnetoresistance in WTe_2. *Phys. Rev. Lett.* **2014**, *113*, 216601.
(12) Mun, E.; Ko, H.; Miller, G. J.; Samolyuk, G. D.; Bud'ko, S. L.; Canfield, P. C. Magnetic field effects on transport properties of $PtSn_4$. *Phys. Rev. B: Condens. Matter Mater. Phys.* **2012**, *85*, 035135.
(13) Zhang, L. Z.; Wang, Z. F.; Du, S. X.; Gao, H. J.; Liu, F. Prediction of a Dirac state in monolayer TiB_2. *Phys. Rev. B: Condens. Matter Mater. Phys.* **2014**, *90*, No. 161402(R).
(14) Zhang, H.; Li, Y.; Hou, J.; Du, A.; Chen, Z. Dirac State in the FeB_2 Monolayer with Graphene-Like Boron Sheet. *Nano Lett.* **2016**, *16*, 6124−6129.
(15) Xie, S.-Y.; Li, X.-B.; Tian, W. Q.; Chen, N.-K.; Zhang, X.-L.; Wang, Y.; Zhang, S.; Sun, H.-B. First-principles calculations of a robust two-dimensional boron honeycomb sandwiching a triangular molybdenum layer. *Phys. Rev. B: Condens. Matter Mater. Phys.* **2014**, *90*, 035447.
(16) Zhang, L.; Yu, J.; Yang, M.; Xie, Q.; Peng, H.; Liu, Z. Janus graphene from asymmetric two-dimensional chemistry. *Nat. Commun.* **2013**, *4*, 1443.
(17) Lu, A. Y.; et al. Janus monolayers of transition metal dichalcogenides. *Nat. Nanotechnol.* **2017**, *12*, 744−749.
(18) Zhang, J.; et al. Janus Monolayer Transition-Metal Dichalcogenides. *ACS Nano* **2017**, *11*, 8192−8198.
(19) Su, S. H.; Hsu, Y. T.; Chang, Y. H.; Chiu, M. H.; Hsu, C. L.; Hsu, W. T.; Chang, W. H.; He, J. H.; Li, L. J. Band gap-tunable molybdenum sulfide selenide monolayer alloy. *Small* **2014**, *10*, 2589−94.
(20) Dong, L.; Lou, J.; Shenoy, V. B. Large In-Plane and Vertical Piezoelectricity in Janus Transition Metal Dichalchogenides. *ACS Nano* **2017**, *11*, 8242−8248.
(21) Yin, W.-J.; Wen, B.; Nie, G.-Z.; Wei, X.-L.; Liu, L.-M. Tunable dipole and carrier mobility for a few layer Janus MoSSe structure. *J. Mater. Chem. C* **2018**, *6*, 1693−1700.
(22) Hu, T.; Hong, J.; Zhao, G.; Wu, J.; Stroppa, A.; Ren, W. Intrinsic and anisotropic Rashba spin splitting in Janus transition-metal dichalcogenide monolayers. *Phys. Rev. B: Condens. Matter Mater. Phys.* **2018**, *97*, 235404.
(23) Li, F.; Wei, W.; Zhao, P.; Huang, B.; Dai, Y. Electronic and Optical Properties of Pristine and Vertical and Lateral Heterostructures of Janus MoSSe and WSSe. *J. Phys. Chem. Lett.* **2017**, *8*, 5959−5965.
(24) Peng, R.; Ma, Y.; Zhang, S.; Huang, B.; Dai, Y. Valley Polarization in Janus Single-Layer MoSSe via Magnetic Doping. *J. Phys. Chem. Lett.* **2018**, *9*, 3612−3617.
(25) Ma, X.; Wu, X.; Wang, H.; Wang, Y. A Janus MoSSe monolayer: a potential wide solar-spectrum water-splitting photocatalyst with a low carrier recombination rate. *J. Mater. Chem. A* **2018**, *6*, 2295−2301.
(26) Ji, Y.; Yang, M.; Lin, H.; Hou, T.; Wang, L.; Li, Y.; Lee, S.-T. Janus Structures of Transition Metal Dichalcogenides as the Heterojunction Photocatalysts for Water Splitting. *J. Phys. Chem. C* **2018**, *122*, 3123−3129.
(27) Kresse, G.; Hafner, J. Ab initiomolecular dynamics for liquid metals. *Phys. Rev. B: Condens. Matter Mater. Phys.* **1993**, *47*, 558−561.
(28) Kresse, G.; Furthmüller, J. Efficient iterative schemes for ab initio total-energy calculations using a plane-wave basis set. *Phys. Rev. B: Condens. Matter Mater. Phys.* **1996**, *54*, 11169−11186.
(29) Blöchl, P. E. Projector augmented-wave method. *Phys. Rev. B: Condens. Matter Mater. Phys.* **1994**, *50*, 17953−17979.
(30) Perdew, J. P.; Burke, K.; Ernzerhof, M. Generalized gradient approximation made simple. *Phys. Rev. Lett.* **1996**, *77*, 3865−3868.
(31) Gonze, X.; Lee, C. Dynamical matrices, Born effective charges, dielectric permittivity tensors, and interatomic force constants from density-functional perturbation theory. *Phys. Rev. B: Condens. Matter Mater. Phys.* **1997**, *55*, 10355−10368.
(32) Togo, A.; Oba, F.; Tanaka, I. First-principles calculations of the ferroelastic transition between rutile-type and $CaCl_2$-type SiO_2 at high pressures. *Phys. Rev. B: Condens. Matter Mater. Phys.* **2008**, *78*, 134106.

DOI: 10.1021/acs.jpcc.8b10371
J. Phys. Chem. C 2018, 122, 28423−28430

(33) Tang, H.; Ismail-Beigi, S. Novel precursors for boron nanotubes: the competition of two-center and three-center bonding in boron sheets. *Phys. Rev. Lett.* **2007**, *99*, 115501.
(34) Zhang, M.; Wang, H.; Wang, H.; Cui, T.; Ma, Y. Structural Modifications and Mechanical Properties of Molybdenum Borides from First Principles. *J. Phys. Chem. C* **2010**, *114*, 6722−6725.
(35) Dawson, W. G.; Bullett, D. W. Electronic structure and crystallography of $MoTe_2$ and WTe_2. *J. Phys. C: Solid State Phys.* **1987**, *20*, 6159.
(36) Malko, D.; Neiss, C.; Viñes, F.; Görling, A. Competition for graphene: graphynes with direction-dependent Dirac cones. *Phys. Rev. Lett.* **2012**, *108*, 086804.
(37) Lv, H. Y.; Lu, W. J.; Shao, D. F.; Liu, Y.; Tan, S. G.; Sun, Y. P. Perfect charge compensation in WTe_2 for the extraordinary magnetoresistance: From bulk to monolayer. *Europhys. Lett.* **2015**, *110*, 37004.
(38) Heyd, J.; Scuseria, G. E.; Ernzerhof, M. Hybrid functionals based on a screened Coulomb potential. *J. Chem. Phys.* **2003**, *118*, 8207−8215.
(39) Hong, X.; Posadas, A.; Zou, K.; Ahn, C. H.; Zhu, J. High-mobility few-layer graphene field effect transistors fabricated on epitaxial ferroelectric gate oxides. *Phys. Rev. Lett.* **2009**, *102*, 136808.
(40) Zheng, Y.; Ni, G. X.; Toh, C. T.; Tan, C. Y.; Yao, K.; Ozyilmaz, B. Graphene field-effect transistors with ferroelectric gating. *Phys. Rev. Lett.* **2010**, *105*, 166602.
(41) Falvo, M. R.; Clary, G. J.; Taylor, R. M.; Chi, V.; Brooks, F. P., Jr; Washburn, S.; Superfine, R. Bending and buckling of carbon nanotubes under large strain. *Nature* **1997**, *389*, 582.

DOI: 10.1021/acs.jpcc.8b10371
J. Phys. Chem. C 2018, 122, 28423−28430